Comparative Analysis, Characterization and Simulation of a Flyback DC-DC Converter Planar Topology Transformer

Gabriel R. Bruzinga, Ademir Pelizari, Jose Alberto Torrico Altuna, Alfeu Sguarezi Filho, and Vinicius Graias

***Abstract*—This work compares two analytical methods (*A* and *B*) for sizing planar topology transformers (PTT) in 20W DC-DC flyback converters, aiming to minimise losses and core volume. In the analytical comparison, method B showed a 6.4% lower volume compared to method A. Structure *B*, with better performance in the analytical step, was modelled by a multiphysics analysis in finite element software, which indicated a slight increase in temperature in the core and windings, with electrical potentials consistent with the number of turns. The magnetostatic analysis showed that the predominant flux density (130-160 mT) was within the adopted reference value (160 mT). The AC resistance calculation showed that the skin and proximity effects contribute about 50% each. A prototype was built and evaluated experimentally, with measurements of DC/AC resistance, frequency response, short-circuit and no-load tests, and transformation ratio. Finally, the closed-loop circuit was simulated with equivalent parameters extracted from the tests.**

Link to graphical and video abstracts, and to code:
https://latamt.ieeer9.org/index.php/transactions/article/view/10754

***Index Terms*—Compact Planar Transformer, Finite Element Method, Flyback Converter**

I. Introduction

HIGHLY efficient energy conversion achieved in compact devices has been fundamental to the continuous growth and profitable development of the consumer products industry and of many others. The main obstacles to obtaining higher efficiency in converters and switching mode power supplies (SMPS), operating at frequencies above 100kHz, are the limitations arising from the construction of conventional ferromagnetic cores and in active windings formed by conventional magnetic wires. However, after the 1990s, the introduction of gallium nitride (GaN) semiconductors boosted research into converters and made it possible to drastically reduce their profile, with the possibility of operating safely at frequencies in the 1MHz range [1]–[5]. This technology, combined with the use of PTT, where the conventional winding manufacturing process is replaced by stamped or printed coils, has resulted in devices that are only a few millimetres high. [6]–[11].

The associate editor coordinating the review of this manuscript and approving it for publication was Diego Rivelino Espinoza Trejo (*Corresponding author: Gabriel Bruzinga).*

Gabriel Bruzinga, A. Pelizari, J. A. T. Altuna, A. S. Filho, and V. Graias are with the Universidade Federal do ABC - UFABC, Brazil (e-mails: gabriel.bruzinga@ufabc.edu.br, ademir.pelizari@ufabc.edu.br, jose.torrico@ufabc.edu.br, alfeu.sguarezi@ufabc.edu.br and vinicius.graias@ufabc.edu.br).

A. TTP Design

Designing a conventional transformer for use in switched converters is still a challenge for even the most experienced designers, even today. Accurately estimating the parameters has been the subject of several studies, using analytical and/or numerical resolution methods. This difficulty is compounded by variations imposed by manufacturing processes, such as variations in stray inductance due to coil construction, which undergoes variations due to the tension applied and its accommodation during construction.

Conventional winding transformers are being replaced by PTTs in various products, including cost-sensitive and high-volume applications. From a manufacturing standpoint, PTT construction is simpler and less dependent on operator skill, ensuring repeatability of device parameters with high production volume. However, their design is not trivial, as there are difficulties in determining their parameters considering the restrictions on the number of turns, the current capacity of the tracks and their accommodation in the physical space allocated to the printed circuit, the distribution of potential in the windings and, due to high frequency, the proximity and skin effects. In this scenario, the evaluation of the best arrangements, not only of the tracks, but also of the combinations of the printed circuit board layers, becomes an aspect to be investigated. The literature associates planar transformers in high-frequency converters and SMPS [12], [13] primarily with a low profile [14], high power density [15], good thermal dissipation as well as the ability to reduce leakage inductance [16], high manufacturing repeatability, and integration of magnetic components.

B. Motivation and Objectives

The motivation for planar-transformer research has evolved substantially over the last decade. The central question is no longer only whether a conventional wound transformer can be replaced by a low-profile PCB structure, but how the magnetic component can be co-designed with the converter so that winding loss, core loss, leakage inductance, parasitic capacitance, insulation, thermal performance, manufacturability, and power density are simultaneously controlled. Recent reviews identify these coupled electromagnetic and thermal effects as the main barriers to extending planar transformers from low- and medium-power converters to high-power, high-frequency applications [17]. This change is reinforced by

wide-bandgap devices, since GaN and SiC switches permit higher switching frequencies and lower semiconductor losses, while transferring a larger fraction of the design burden to the magnetic component.

From a practical design perspective, the main difficulty is therefore not the absence of sizing rules, but the lack of a single methodology that remains sufficiently transparent and reproducible while accounting for the coupled constraints of a planar structure. Manufacturer application notes are useful for initial core and winding selection, but they generally require additional assumptions regarding admissible flux density, loss density, thermal path, conductor arrangement, leakage inductance, and high-frequency resistance. Consequently, two designers using different sizing criteria may obtain distinct core volumes, numbers of turns, copper geometries, and thermal margins for the same electrical specification. This is precisely the motivation for comparing independent analytical procedures before proceeding to finite-element and experimental validation.

Tables I and II summarize the evolution of planar-transformer design and the analytical/numerical strategies adopted in representative studies. Table I combines selected historical milestones with recent state-of-the-art developments, allowing the progression from proof-of-concept planar structures to high-frequency, multi-parameter magnetic co-design to be seen within a single-column comparison.

The historical literature also shows that analytical calculation, two or three-dimensional field simulation, thermal analysis, and prototype characterization have often been treated as separate stages rather than as a unified design workflow, as shown in Table II.

More recent work, especially from 2023 onward, has shifted the state of the art toward application-specific and multi-parameter optimization. At winding level, partially interleaved structures have been optimized to reduce leakage inductance for non-unity turns ratios [25], while termination layout has been shown to contribute appreciably to the AC resistance of high-current PCB matrix transformers [33]. For high-current converters, current sharing among parallel windings has become an explicit design objective; a 30-kW LLC transformer reported in [26] combined analytical current-distribution modeling with loss/volume optimization and experimental validation.

A second research direction is the deliberate use of leakage inductance as a functional element of the converter. Matrix and integrated magnetic structures have been proposed to embed resonant inductance without adding a separate magnetic component. Nabih and Li [34] embedded the resonant inductor into a PCB matrix transformer, whereas Jin *et al.* [28] developed a scalable matrix integrated transformer with controllable leakage inductance for bidirectional resonant conversion. Related work improved PCB utilization and core-flux distribution in integrated transformer–inductor structures, reducing both winding and core losses [35]. These results indicate that leakage inductance should not always be treated as a parasitic quantity; in resonant converters it may instead be a controlled design variable.

A third trend is the co-design of planar magnetics with wide-bandgap converters. In a 3-kW 400-to-48-V LLC converter, geometry, turn number, resonant frequency, matrix transformer, and matrix inductor were jointly optimized, resulting in 98.8% peak efficiency [27]. For automotive applications, integrated planar magnetics have been extended to multi-kilowatt CLLC converters: a three-phase integrated transformer was demonstrated in a 16.5-kW on-board charger [36], and a detailed comparison of integrated planar transformer structures for a 22-kW on-board charger addressed current sharing, leakage-inductance control, flux distribution, manufacturability, and thermal performance [30]. At still higher switching frequency, a 700-kHz GaN-based 1.2-kW converter used an integrated planar transformer to reduce magnetic footprint [31].

TABLE I
REPRESENTATIVE EVOLUTION OF PLANAR AND HIGH-FREQUENCY TRANSFORMER DESIGN

Ref.	Year	f_{sw} (MHz)	P_o (W)	Topology / application	Core feature or main design contribution
[18]	1990	1.0	0.65	Flyback / micro-regulator	Laminated CoZr microtransformer; early demonstration of low-profile magnetic integration.
[19]	1991	32	1.0	Forward / micro-converter	Multilayer CoZrRe structure operating in the multi-MHz range.
[10]	1994	0.5	150	Forward / PTT	RM8/RM10 planar structures; early use of field analysis for planar-transformer design.
[20]	1996	–	≥ 100	SMPS / half-bridge	MnZn 3F3 planar magnetics aimed at scalable flyback/forward power supplies.
[21]	2015	1.0	50	Forward / PTT	E32/6/20, 3F4; analytical sizing combined with 2-D FEM verification.
[22]	2016	0.1	13	HV flyback	ELP22/6/16, N87; analytical design, FEM evaluation, and prototype validation.
[23]	2018	1.0	30	Active-clamp flyback	ER14.5/3/7, 3F4; compact high-frequency planar SMPS implementation.
[24]	2021	0.3	1000	AC–DC / totem-pole PFC	Extension of planar magnetic concepts toward the kilowatt range.
[25]	2023	–	–	Planar transformer	Partially interleaved windings optimized to reduce leakage inductance for non-unity turns ratios.
[26]	2023	–	30000	LLC	Parallel-winding current sharing with coupled loss/volume optimization.
[27]	2023	–	3000	400/48-V LLC	Joint optimization of matrix transformer, matrix inductor, geometry, and resonant frequency.
[28]	2023	–	11000	Bidirectional CLLC	Controllable leakage inductance used as a functional resonant design variable.
[29]	2023	0.2	15000	CLLC / SST	Multi-objective design including insulation, core, winding, and shielding losses.
[30]	2024	–	22000	CLLC / OBC	Comparison of integrated planar structures including current sharing, leakage, flux, and thermal behavior.
[31]	2024	0.7	1200	GaN Zeta / EV	Integrated planar transformer with partial flux cancellation at 700 kHz.
[32]	2025	–	6600	DAB / GaN–SiC	Pareto-based semiconductor–magnetic co-design over a wide operating range.
[17]	2026	–	–	Review / PTT	Unified treatment of winding/core loss, parasitics, thermal constraints, leakage integration, and optimization.

TABLE II
DESIGN AND VALIDATION STRATEGIES IN REPRESENTATIVE PTT STUDIES

Ref.	Analytical Method	Magnetic FEM/FEA	Thermal Analysis	Design Optimization	Experimental Validation
[18]	no	no	no	no	yes
[19]	no	no	no	no	yes
[10]	no	yes	no	no	yes
[20]	no	no	no	no	yes
[21]	yes	yes	no	no	no
[22]	yes	yes	no	no	yes
[23]	yes	no	no	no	yes
[24]	yes	no	no	no	yes
[25]	yes	yes	no	yes	yes
[26]	yes	yes	no	yes	yes
[27]	yes	yes	yes	yes	yes
[28]	yes	yes	no	yes	yes
[29]	yes	yes	yes	yes	yes
[30]	yes	yes	yes	yes	yes
[31]	yes	no	no	yes	yes
[32]	yes	no	no	yes	yes
[17]	yes	yes	yes	yes	–

More recently, a reconfigurable DAB converter combining bidirectional GaN, SiC devices, and a Pareto-optimized planar transformer demonstrated the increasing coupling between semiconductor selection, operating range, and magnetic design [32]. Beyond low-voltage applications, high-frequency transformer research has also emphasized insulation coordination and multi-objective loss/volume optimization. Li *et al.* [29] included medium-voltage insulation, core loss, winding loss, shielding loss, and fabrication constraints in the transformer design for a 200-kHz CLLC solid-state-transformer module. This broader perspective is consistent with the recent review in [17], which identifies winding loss, core loss, parasitic capacitance, thermal management, leakage-inductance integration, and optimization as strongly coupled design problems.

The recent entries in Table I clarify that the current state of the art is dominated by resonant LLC/CLLC and DAB converters in the kilowatt range, where planar magnetics are increasingly optimized together with the converter. These studies achieve remarkable efficiency and power density, but their design variables and objectives are strongly topology dependent: controlled leakage inductance, parallel-winding current sharing, magnetic integration, EMI, and wide-voltage-range soft switching are often more important than the classical transformer-sizing problem itself. Conversely, comparatively fewer studies examine how different analytical core-sizing methodologies affect the complete design trajectory of a low-power planar flyback transformer and then validate that choice using consistent electromagnetic, thermal, experimental, and converter-level analyses. This paper addresses this complementary gap. It does not seek to surpass the power density of recent multi-kilowatt resonant converters. Instead, its contribution is methodological: two independent analytical procedures are applied to the same specification for a 20 W, 100 kHz CCM flyback converter, enabling a comparison of the influence of the design criteria on core volume, number of turns, flux density, winding geometry and losses, under identical requirements. The selected design is then subjected to a series of 3D simulations under magnetostatic, electrostatic and thermostatic conditions, followed by the fabrication of a prototype and its characterisation through measurements and parameter tests, frequency response analysis, and converter-level simulation using experimentally obtained parameters. Thus, the specific objectives of this work are:

1) To compare 2 analytical planar-transformer sizing methodologies under the same specifications;
2) To quantify core and planar-winding losses in absolute power units, including the contribution of DC resistance, skin effect, and proximity effect;
3) To verify magnetic flux density, electric-potential distribution, current-density effects, and temperature distribution using three-dimensional finite-element models;
4) Experimentally characterize the selected transformer, comparing analytical and measured electrical parameters; and
5) To identify the practical tradeoff between reduced magnetic-core volume and total transformer efficiency, thereby establishing which loss mechanism limits further improvement of the proposed design.

This also defines the principal limitation and contribution of the proposed methodology. Unlike recent multi-objective optimization frameworks, the present approach does not yet perform a simultaneous global optimization of geometry, parasitic capacitance, leakage inductance, EMI, and thermal resistance. Its advantage is that each design assumption and loss mechanism remains traceable from the analytical stage to the numerical and experimental results. The methodology therefore provides a reproducible baseline from which more advanced multi-objective optimization can subsequently be developed.

II. PLANAR WINDING LOSSES

In alternating current, the total electrical resistance at the operating frequency will be the sum of the resistances due to the skin and proximity effects, i.e.:

$$R_{(ac,f)} = R_{(ac,skin)} + R_{(ac,prox)} \tag{1}$$

The current density in the conductor behaves exponentially and decreases as the distance to the centre of the track decreases [37]. The penetration depth of the alternating current in the copper track (δ) is calculated by (2):

$$\delta = \sqrt{\frac{2}{\mu_0 \cdot \sigma \cdot \omega}} \tag{2}$$

This situation (Skin Effect) can be seen in Fig.1.

In (2), ω is the angular velocity (rad/s), μ_0 is the magnetic permeability of the material in vacuum and σ is the conductivity of copper ($5.8 \cdot 10^7$ S/m).

Designating the skin factor as $K_{(skin)}$, we can define the relationship between the DC and AC resistances as:

$$R_{(ac,skin)} = K_{(skin)} \cdot R_{(dc)} \tag{3}$$

The AC electrical resistance attributed to the skin effect can be determined using the Dowell's equation (4) [38]:

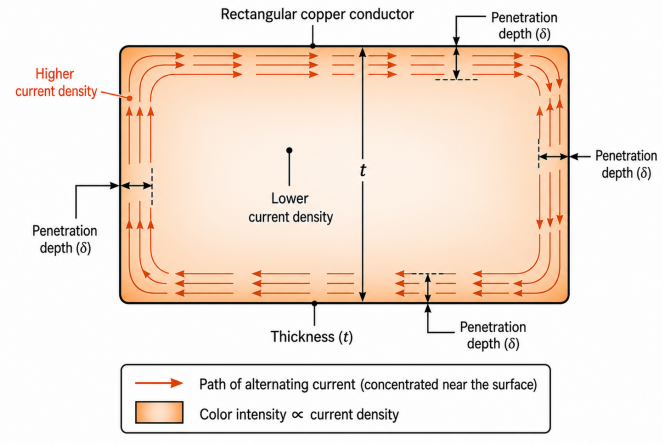


Fig. 1. Skin Effect in a Conductor Under High-Frequency Current, Illustrating the Current Path and the Axial Current Density Distribution.

$$R_{(ac,skin)} = \frac{\xi}{2} \cdot \frac{\sinh(\xi) + \sin(\xi)}{\cosh(\xi) - \cos(\xi)} \cdot R_{(dc)} \tag{4}$$

In (4), ξ is the ratio between the conductor thickness t and the penetration depth δ, defined in (5):

$$\xi = \frac{t}{\delta} \tag{5}$$

In the proposed method [38], square conductors of equivalent area to circular ones are grouped together, forming a conductive sheet, representing a winding layer, stretched in the direction of the thickness, forming a sheet of uniform height, however presenting a porous surface, as in Fig.2.

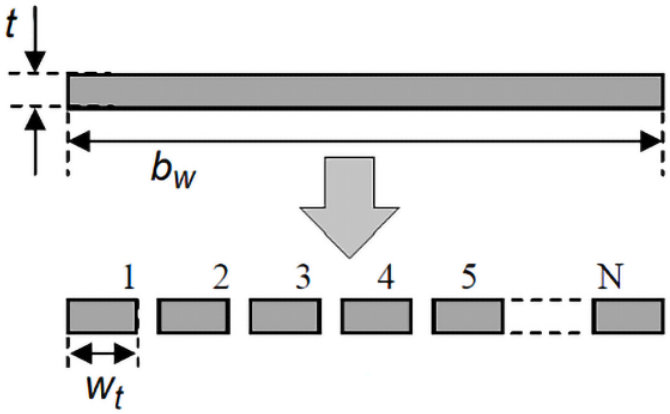


Fig. 2. Porosity Factor Representation of a Conductive Sheet Formed by Grouped Square Conductors, Showing the Resulting Porous Surface After Stretching in the Thickness Direction.
Adapted [38]

Therefore, a porosity factor η is added to correct the DC resistance of the original winding [39], determined by:

$$\eta = \frac{N \cdot w_t}{b_w} \tag{6}$$

In a multi-layer winding made up of rectangular or circular conductors, it can be seen that the alternating current flowing in one conductor will induce eddy currents in the adjacent conductor. In this way, the ratio between the AC and DC resistances, due to the proximity effect, becomes:

$$K_{(prox)} = \frac{R_{(ac,prox)}}{R_{(dc)}} \tag{7}$$

This ratio can be estimated using Dowell's equation:

$$\frac{R_{(ac,prox)}}{R_{(dc)}} = \frac{\xi}{2} \cdot (2m-1)^2 \cdot \frac{\sinh(\xi) - \sin(\xi)}{\cosh(\xi) + \cos(\xi)} \tag{8}$$

where m is given by

$$m = \left| \frac{\text{mmf}_{(k)}}{\text{mmf}_{(k)} - \text{mmf}_{(k-1)}} \right| \tag{9}$$

With the inclusion of the porosity factor, the AC resistance due to the proximity effect in the winding layer, for the corresponding m factor, is given by:

$$\frac{R_{(ac,prox)}}{R_{(dc)}} = \xi' \cdot \frac{2}{3} \cdot (m^2 - 1) \cdot \frac{\sinh(2\xi') - \sin(2\xi')}{\cosh(2\xi') + \cos(2\xi')} \tag{10}$$

The AC electrical resistance of a given k winding layer, due to the proximity effect, is estimated by *Dowell* (8), based on the ratio between the magnetomotive force (mmf) of the target layer and its subtraction from the mmf of the previous layer $(k-1)$.

A. Core Losses

The core losses due to magnetic hysteresis are related to the material's characteristic BH curve and as a function of the maximum flux density. Also, eddy current losses occur in magnetic cores [40]. Both of them can be calculated according to the equations (11) and (12) respectively, as:

$$P_H = k_H \cdot f \cdot V_c \cdot B_{max}^{\alpha} \tag{11}$$

$$P_E = k_E \;.\; f^2 \;.\; V_c \;.\; B_{max}^2 \tag{12}$$

In (11) and (12), V_c is the core volume, f is the operating frequency and the factors k_H, k_E (both in mW/cm^3) and α are obtained from experimental measurements performed by manufacturers, with typical values ranging from 10^{-2} to 10^{1} for k_H, 10^{-12} to 10^{-4} for k_E, and 1.3 to 2.2 for α. Table III shows the coefficients for material 3C95.

III. Analytical Method

This section presents two methodologies for sizing a PTT with Output Power (P_o) of 20 W, Output Voltage (V_o) of 10 V, Output Current (I_o) of 2 A, Output Impedance (Z_o) of 5 Ω and Switching Frequency (f_{sw}) of 100 kHz.

TABLE III
STEINMETZ COEFFICIENTS — 3C95.

k_H	k_E	α
0.4732179	1.174614×10^{-12}	2.87

A. Type A Methodology [41]

Fig. 3 shows the flowchart of the steps in PTT sizing, for applications with a single secondary winding.

The representation of the current and voltage waveforms in the primary switch Q, operating in CCM, is shown in Fig.4.

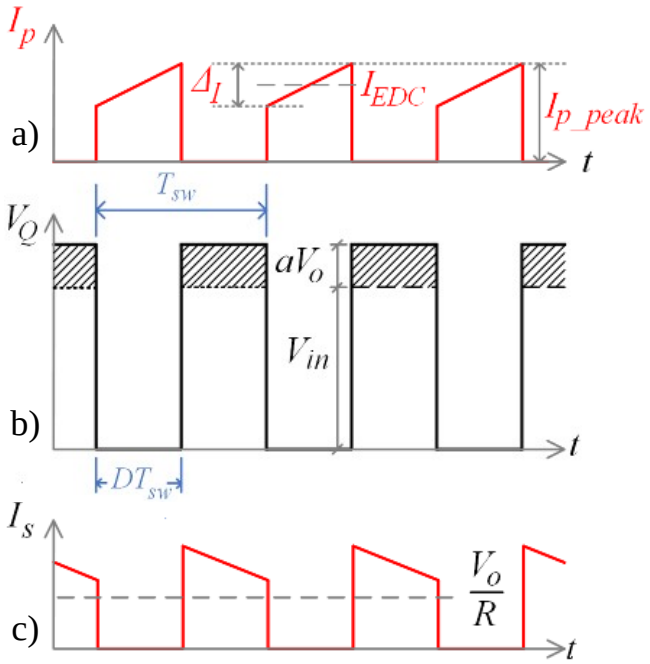


Fig. 4. Current and Voltage Waveforms of Switch Q Operating in CCM - a) primary current b) switch voltage c) secundary current. Adapted [42]

In Fig. 4, I_p is the primary current, I_s is the secondary current and V_Q is the voltage across the switch. The maximum duty cycle D_{max} is obtained by adopting the conversion ratio a, as far as the design allows, as follows:

$$D_{max} = \frac{a \cdot V_o}{V_{in_min} + a \cdot V_o} \tag{13}$$

The effective current values can be obtained from (14):

$$I_{EDC} = \frac{P_{in}}{V_{in_min} \cdot D_{max}} \tag{14}$$

In (14), I_{EDC} is the average DC current in the half-cycle conduction of the primary switch. The relationship between the core's areas and the design variables is shown in (15):

$$A_w A_e \geq \frac{(V_{in_min} \cdot D_{max})^2 \cdot I_{p_peak} \cdot I_{p_rms}}{2 \cdot P_{in} \cdot f_{sw} \cdot K_{RF} \cdot K_w \cdot B_{max} \cdot J} \cdot 10^6 \tag{15}$$

In (15), the left-hand side is the product area in mm^4. On the right-hand side K_w is the core window utilization factor, B_{max} is the maximum flux density adopted, J is the current density in the conductors and the minimum number of turns in the primary is (16), according to:

$$N_{p_min} = \frac{(V_{in_min} \cdot D_{max})^2 \cdot I_{p_peak}}{2 \cdot P_{in} \cdot f_{sw} \cdot K_{RF} \cdot B_{max} \cdot A_e} \cdot 10^6 \tag{16}$$

The number of secondary turns is determined by (17):

$$N_s = \frac{N_{p_min} \cdot V_o \cdot (1 - D_{max})}{V_{in_min} \cdot D_{max}} \tag{17}$$

The calculated parameters using equations (13) to (17) are shown in Table IV.

TABLE IV
RESULTS OBTAINED WITH TYPE A METHODOLOGY

Core: 43618EC — B_{max}: 160 mT					
Calculated			**Adopted**		
I_{EDC}	1.47	A	*Op. Mode*	CCM	
ΔI	0.76	A	D_{max}	0.82	
I_{p_peak}	1.85	A	V_{in_min}	20.8	V
I_{p_rms}	1.34	A	P_{in}	25	W
$A_w A_e$	3467	mm^4	K_{RF}	0.26	
N_{p_min}	19.1	Turns	K_w	0.2	
N_s	2	Turns	J	5	A/mm^2
I_{s_rms}	5.96	A	A_e	135	mm^2
a	9.48		B_{max}	0.16	T

B. Type B Methodology

The temperature rise in the PTT is such that it can cause damage to the transformer itself. These losses must be limited by the temperature rise and the magnetic flux density. Fig. 5 shows the methodology.

The core loss density can be estimated in (18). In (19), the coefficients are specific to each type of material and are adjusted so that C_T is equal to unity at operating temperature of 100°C, as follows:

$$P_{core} = C_m \cdot C_T \cdot f_{sw}^x \cdot B_{max}^y \tag{18}$$

$$C_T = c_{t0} - c_{t1} \cdot T + c_{t2} \cdot T^2 \tag{19}$$

The parameters C_m, x, y, c_{t0}, c_{t1} and c_{t2} are shown in Table V, for some of power ferrites available.

TABLE V
MATERIAL'S COEFFICIENTS

Material	f_{sw}	C_m	**x**	**y**	c_{t2}	c_{t1}	c_{t0}
3C30	100k–200k	0.00713	1.42	3.02	0.000400	0.068	3.8
3C90	20k–200k	0.00320	1.46	2.75	0.000165	0.031	2.45
3C94	20k–200k	0.00237	1.46	2.75	0.000165	0.031	2.45
3F3	100k–300k	0.00025	1.63	2.45	0.000079	0.010	1.26
3C95	20k–150k	0.09216	1.04	2.44	0.000046	0.0079	1.33

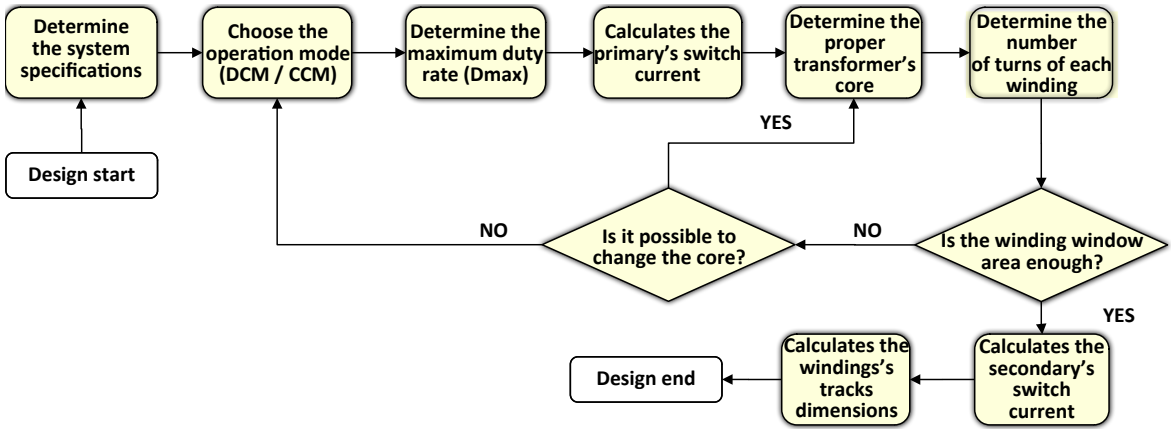


Fig. 3. Type A Methodology: PTT Sizing Steps for Single Secondary Winding Applications.

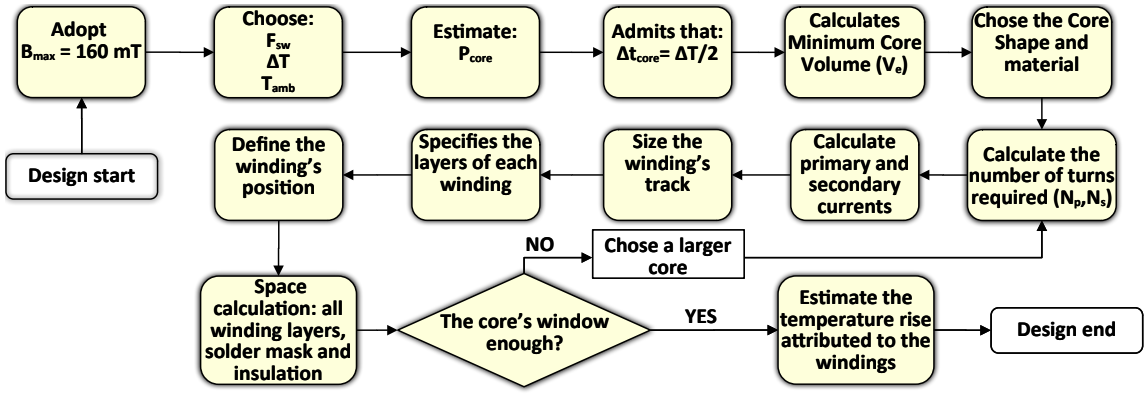


Fig. 5. Type B Methodology: PTT Sizing Procedure Constrained by Temperature Rise and Magnetic Flux Density.

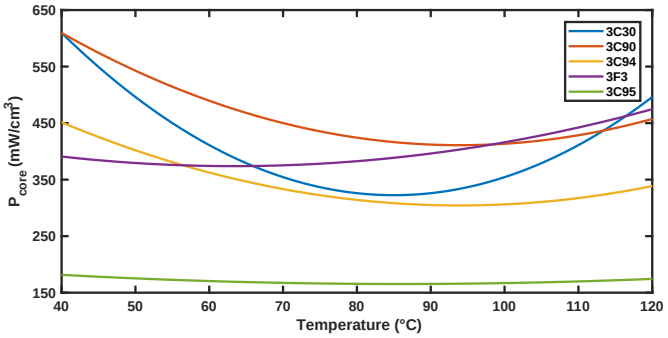


Fig. 6. Power Loss Density at 100kHz and 160mT.

Under the conditions set by design and with each material's coefficients, the loss curves were obtained as a function of temperature, as shown in Fig.6.

In (20), the maximum density of core losses is determined as a function of the effective volume and the permitted temperature rise.

$$P_{core_max} = \frac{12 \cdot \Delta T}{\sqrt{V_e}} \tag{20}$$

In (20), P_{core_max} is expressed in mW/cm³, V_e is the effective core's volume in cm³. By replacing P_{core} in (18) with P_{core_max}, we can isolate B_{max}, thereby determining its value as follows:

$$B_{max} = \left(\frac{12 \cdot \Delta T}{C_m \cdot C_T \cdot f_{sw}^{x} \cdot \sqrt{V_e}} \right)^{\frac{1}{y}}. \tag{21}$$

Using (21) it's possible to check the minimum volume required for the core, depending on the material chosen, using the flux density adopted according to Fig.7.

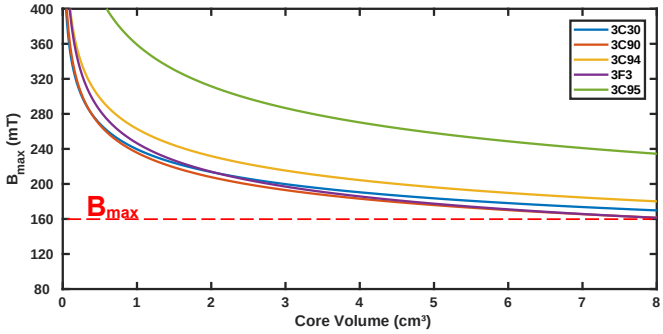


Fig. 7. Maximum Flux Density at 100kHz and 100°C.

In (22), ΔT_{core} represents the isolated core's contribution to the temperature rise, as follows:

$$\Delta T_{core} = \frac{P_{core}}{P_{core_max}} \cdot \frac{\Delta T}{2} \tag{22}$$

Once the core has been chosen, the number of turns of the primary and secondary windings is calculated respectively by:

$$N_p = \frac{V_{in_min} \cdot D}{2 \cdot f_{sw} \cdot K_{RF} \cdot B_{max} \cdot A_e} \cdot 10^6 \tag{23}$$

$$N_s = \frac{N_p \cdot V_o \cdot (1 - D)}{V_{in_min} \cdot D}. \tag{24}$$

The calculated parameters using equations (18) to (24) are shown in Table VI.

TABLE VI
RESULTS OBTAINED WITH TYPE B METHODOLOGY

Calculated				Adopted	
P_{core}	180.8	mW/cm³	*Material*	3C95	
P_{core_max}	181.1	mW/cm³	C_T	1	
B_{max}	160	mT	ΔT	35	°C
ΔT_{core}	17.5	°C	*Core*	E32/6/20	
N_p	18	Turns	V_e	5.38	cm³
N_s	1.9	Turns	A_e	129	mm²

IV. SIZING THE WINDING TRACKS

The maximum width of the tracks per layer [23] can be estimated, according to (25):

$$w_t = \frac{b_w - s \cdot (N + 1)}{N} \tag{25}$$

In (25) w_t represents the width of the track, b_w is the width available in the core to accommodate the windings, s is the spacing between the tracks and N represents the number of turns; these variables are shown in Fig.12.

The expression in (26) corresponds to the area of the square of the primary and secondary bands [22]:

$$A_w = \frac{I_{rms}}{J} \tag{26}$$

V. RESULTS OBTAINED FROM THE METHODOLOGIES

Table VII shows the results obtained in methodologies A and B. Based on the analytical results, the geometry studied in B's methodology was chosen to be simulated using numerical methods and the simulation results are also shown in the same table.

The results obtained with the estimated resistances for the primary and secondary windings used the values adopted in Table VIII for both windings.

Table IX shows the values calculated for the primary winding.

The contribution of the proximity effect to the total AC electrical resistance was estimated by assigning a range of values to the m factor, since the interaction of the magnetic field between the layers would require the investigation of a numerical method for determining this factor, which is beyond the scope and objective of this work. Table X shows the calculated AC resistance values due to the skin effect and proximity effect in the primary winding.

Fig. 9 illustrates the variation in AC resistances due to skin and proximity effects as a function of the m factor, in primary

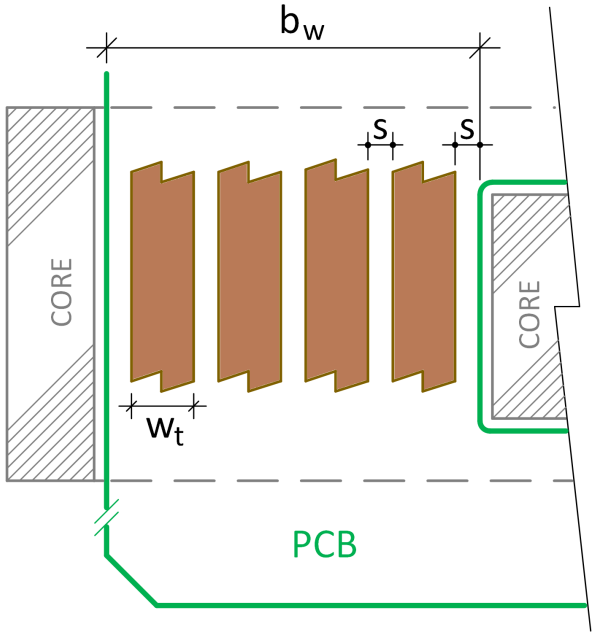


Fig. 8. Layout of the PCB Tracks and the Winding Parameters Used in the Track-Width Calculation.

TABLE VII
COMPARISON OF METHODOLOGIES A AND B

Item	Type A Met.	Type B Met.	Numeric
Operation mode	CCM	CCM	CCM
Core type	43618EC	E32/6/20	E32/6/20
Core material	3C95	3C95	3C95
Core effective area	135 mm²	129 mm²	129 mm²
Core volume	5.75 cm³	5.38 cm³	5.38 cm³
Primary turns (N_p)	19.1	18	18
Secondary turns (N_s)	2.0	1.9	2.0
Track thickness	200 μm	200 μm	200 μm
Primary turns by layer	6	6	6
Secondary turns by layer	1	1	1

TABLE VIII
ADOPTED VALUES

Parameter	Adopted
Switching frequency (f_{sw})	100 kHz
Copper resistivity at 25 °C (ρ)	$1.724 \cdot 10^{-6}$ Ωcm
Magnetic permeability (μ_0)	$1.257 \cdot 10^{-6}$
Core's window (b_w)	9.21 mm
Track thickness (t)	200 μm

TABLE IX
PRIMARY SIDE WINDING PARAMETERS

Parameter	Calculated
Penetration depth (δ)	209 μm
Track width (w_{t_p})	1.30 mm
Thickness / depth ratio (ξ)	0.9571
Turns by layer (N)	6
Porosity factor (η)	0.8469
Correction of ξ (ξ')	0.8807

TABLE X
AC RESISTANCE IN PRIMARY SIDE

Parameter	Calculated
DC resistance — $R_{1(dc)}$	0.912 Ω
Skin factor — $K_{1(skin)}$	1.052
Skin AC resistance — $R_{1(ac,skin)}$	0.960 Ω
m factor	1.87
Proximity factor — $K_{1(prox)}$	0.963
Proximity AC resistance — $R_{1(ac,prox)}$	0.878 Ω

side.

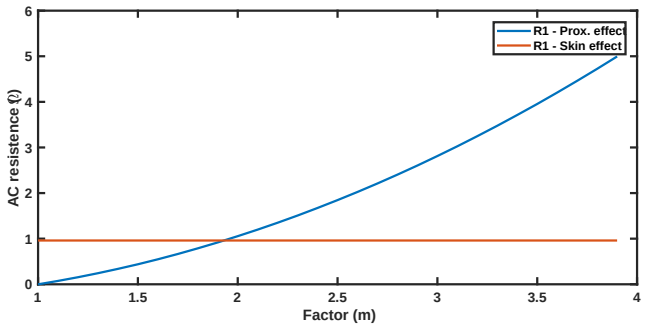


Fig. 9. Estimated AC Resistances in the Primary Side as a Function of the m Factor, Showing Skin and Proximity Effects.

Table XI shows the values calculated for the secondary winding.

TABLE XI
SECONDARY SIDE WINDING PARAMETERS

Parameter	Calculated
Penetration depth (δ)	209 μm
Track width (w_{t_s})	8.81 mm
Thickness / depth ratio (ξ)	0.9571
Turns by layer (N)	1
Porosity factor (η)	0.9566
Correction of ξ (ξ')	0.9361

Table XII shows the calculated AC resistance values due to the skin effect and proximity effect in the secondary winding.

TABLE XII
AC RESISTANCE IN SECONDARY SIDE

Parameter	Calculated
DC resistance — $R_{2(dc)}$	14.34 mΩ
Skin factor — $K_{2(skin)}$	1.0663
Skin AC resistance — $R_{2(ac,skin)}$	15.29 mΩ
m factor	2.01
Proximity factor — $K_{2(prox)}$	1.3889
Proximity AC resistance — $R_{2(ac,prox)}$	19.92 mΩ

Fig. 10 illustrates the variation in AC resistances due to skin and proximity effects as a function of the m factor, in secondary side.

A. Detailed Loss and Transformer Efficiency

The Type B methodology originally provides the core loss mainly as a volumetric density. For the selected E32/6/20 core, the conversion to watts follows directly from (18). At the design point, $p_v = 180.8$ mW/cm^3 and $V_e = 5.38$ cm^3, therefore

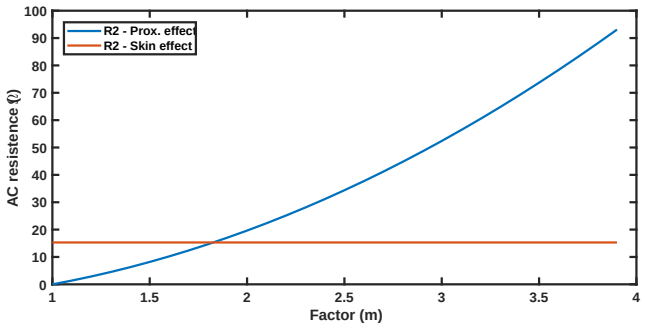


Fig. 10. Estimated AC Resistances in the Secondary Side as a Function of the m Factor, Showing Skin and Proximity Effects.

$$P_{core} = \frac{180.8 \times 5.38}{1000} = 0.9727 \text{ W} \tag{27}$$

In the same way, the maximum loss density imposed by the thermal criterion corresponds to

$$P_{core,max} = \frac{181.1 \times 5.38}{1000} = 0.9743 \text{ W} \tag{28}$$

Thus, the selected operating point uses approximately 99.83% of the core-loss limit defined by the Type B thermal criterion. For the windings, the effective AC resistances at 100 kHz are obtained from the skin and proximity contributions already calculated in Tables X and XII:

$$R_{1,ac} = R_{1,ac,skin} + R_{1,ac,prox} \tag{29}$$
$$= 0.960 + 0.878 = 1.838\ \Omega \tag{30}$$
$$R_{2,ac} = R_{2,ac,skin} + R_{2,ac,prox} \tag{31}$$
$$= 0.01529 + 0.01992 = 0.03521\ \Omega \tag{32}$$

Using the RMS currents of the nominal CCM operating point, $I_{p,rms} = 1.34$ A and $I_{s,rms} = 5.96$ A, the copper losses are:

$$P_{Cu,p} = I_{p,rms}^2 R_{1,ac} = 1.34^2(1.838) = 3.300 \text{ W} \tag{33}$$
$$P_{Cu,s} = I_{s,rms}^2 R_{2,ac} = 5.96^2(0.03521) = 1.251 \text{ W} \tag{34}$$
$$P_{Cu} = P_{Cu,p} + P_{Cu,s} = 4.551 \text{ W} \tag{35}$$

To avoid double counting, it is useful to separate the DC loss, the incremental skin-effect loss, and the proximity-effect loss. Since $R_{ac,skin}$ already contains the DC-resistance baseline in Dowell's formulation, the incremental skin term is $R_{ac,skin} - R_{dc}$. Consequently:

$$P_{Cu,dc} = I_{p,rms}^2 R_{1,dc} + I_{s,rms}^2 R_{2,dc} = 2.147 \text{ W} \tag{36}$$
$$P_{skin,add} = I_{p,rms}^2 (R_{1,ac,skin} - R_{1,dc}) \tag{37}$$
$$+ I_{s,rms}^2 (R_{2,ac,skin} - R_{2,dc}) = 0.120 \text{ W} \tag{38}$$
$$P_{prox} = I_{p,rms}^2 R_{1,ac,prox} + I_{s,rms}^2 R_{2,ac,prox} = 2.284 \text{ W} \tag{39}$$

The complete analytical transformer loss is therefore:

$$P_{loss,tr} = P_{core} + P_{Cu} = 0.973 + 4.551 = 5.524 \text{ W} \quad (40)$$

Considering 20 W delivered by the transformer secondary to the converter output stage and excluding semiconductor, rectifier, snubber, gate-drive and capacitor losses, the transformer-only efficiency is:

$$\eta_{tr} = \frac{P_o}{P_o + P_{loss,tr}} \times 100 = \frac{20}{20 + 5.524} \times 100 = 78.36\%. \quad (41)$$

Table XIII summarizes the loss distribution. The analytical result indicates that winding losses dominate the total transformer loss at the rated operating point.

TABLE XIII
DETAILED TYPE B LOSS BUDGET AT 100 KHZ

Loss component	Loss (W)	Share of total (%)
Core, P_{core}	0.973	17.61
Primary copper, $P_{Cu,p}$	3.300	59.75
Secondary copper, $P_{Cu,s}$	1.251	22.64
Total copper, P_{Cu}	4.551	82.39
Total transformer, $P_{loss,tr}$	5.524	100.00
Transformer efficiency, η_{tr}		78.36%

As an experimental check, the measured primary resistance is 1.830 Ω. The secondary resistance reflected to the primary is 3.047 Ω. Using the manufactured turns ratio $a = N_p/N_s = 18/2 = 9$, the corresponding secondary resistance is $3.047/9^2 = 37.62$ mΩ. With the same RMS currents, the measured-resistance copper loss is approximately 4.622 W. Combining it with the analytical core loss gives 5.595 W and an estimated transformer-only efficiency of 78.14%, close to the analytical value in (41).

B. 1D Model Extrapolation

The flowchart in Fig. 11 summarises the steps carried out for the extrapolation of $1D$ method.

Effective Gap

From the ON-state ramp:

$$\Delta I = \frac{V_{in,min} D}{L_m f_s} \quad (42)$$

so that:

$$L_m = \frac{20.8(0.82)}{0.76(100 \times 10^3)} = 224.42\mu\text{H} \quad (43)$$

If the reluctance is dominated by the gap:

$$g_{eff} \simeq \frac{\mu_0 N_p^2 A_e}{L_m} = 0.234\text{mm} \quad (44)$$

This g_{eff} is used only in the 2D extension; it is a quantity deduced from the current ripple, not a gap value explicitly stated in the original table.

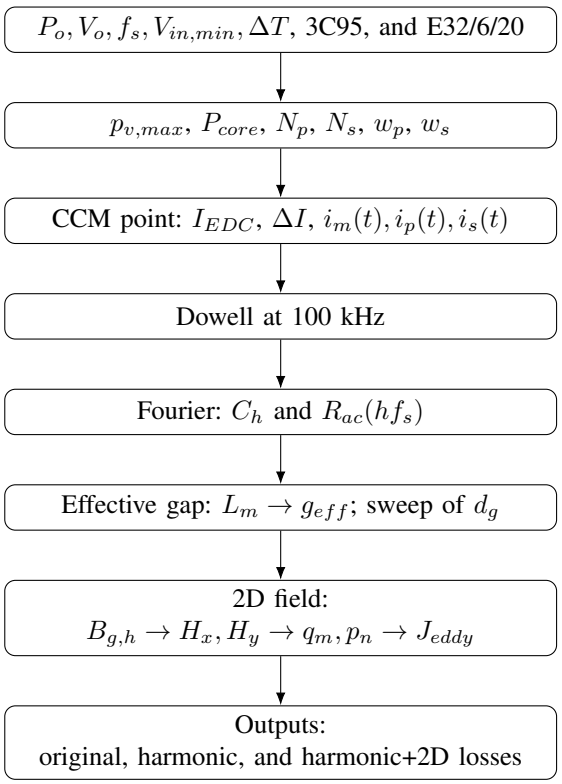


Fig. 11. Flowchart of the code for the 20 W case.

Harmonic Refinement

The original Methodology B applies a resistance evaluated at 100 kHz to the total RMS current. In the harmonic extension,

$$i(t) = I_0 + \sum_{h=1}^{N_h} \text{Re}\{\underline{I}_h e^{jh\omega_s t}\}, \quad (45)$$

and

$$P_{Cu} = R_{dc} I_0^2 + \sum_{h=1}^{40} |I_{h,rms}|^2 R_{ac}(hf_s). \quad (46)$$

The 40-harmonic sum implemented gives

$$P_{Cu,harm} = 4.2871 \text{ W} \quad (47)$$

before the two-dimensional correction. The corresponding efficiency is

$$\eta_{tr,harm} = 79.18\% \quad (48)$$

The difference from 4.551W does not imply an error in Methodology B; it represents a change in modeling level because each temporal component now "sees" its own AC resistance.

2D Extension

The effective area $A_e = 129mm^2$ and the nominal depth of $20.32mm$ of the E32/6/20 core yield an effective pole-face width of approximately

$$a_g \simeq \frac{129}{20.32} = 6.35\text{mm} \quad (49)$$

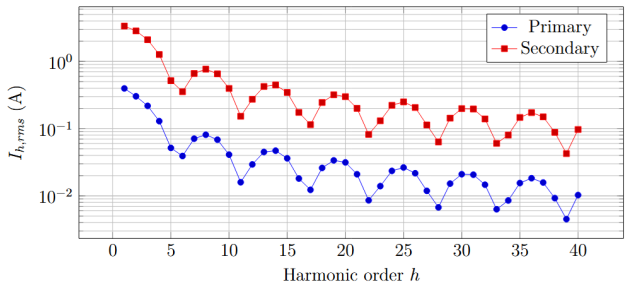


Fig. 12. Spectrum of the CCM Currents Reconstructed from the Operating Point of Methodology B.

The quantity that is not explicitly specified in the original dataset is the distance d_g between the gap edge and the track. Rather than assigning an arbitrary value to the design, it was performed the sweep

$$d_g = 0.2;\ 0.5;\ 1.0;\ 1.5;\ 2.0;\ 2.5;\ 3.0\ \text{mm}. \tag{50}$$

Parametric 2D Result

For each harmonic of the magnetizing current, $B_{g,h}$ is calculated, followed by H_x and H_y using the magnetic-pole model, and finally the modal diffusion in the copper. The additional loss is

$$\Delta P_{gap} = \sum_h \frac{L}{\sigma} \int_A |J_{eddy,h}(x,y)|^2 \mathrm{d}A. \tag{51}$$

TABLE XIV
SENSITIVITY OF THE 2D CORRECTION TO THE TRACK-TO-GAP DISTANCE

d_g (mm)	$\Delta P_{g,p}$ (W)	$\Delta P_{g,s}$ (W)	ΔP_g (W)	η_{tr} (%)
0.2	2.8095	0.3194	3.1289	70.45
0.5	0.4395	0.0527	0.4922	77.66
1	0.0938	0.0108	0.1046	78.85
1.5	0.0373	0.004	0.0413	79.05
2	0.0191	0.0019	0.021	79.11
2.5	0.0112	0.0011	0.0123	79.14
3	0.0071	0.0007	0.0078	79.15

At the illustrative point $d_g = 1\,\text{mm}$,

$$\Delta P_{gap,2D} = 0.1046\ \text{W} \tag{52}$$

Adding it to the harmonic model,

$$P_{loss,tr} = P_{core} + P_{Cu,harm} + \Delta P_{gap,2D}, \tag{53}$$

and the efficiency becomes approximately

$$\eta_{tr} = 78.85\% \tag{54}$$

This $d_g = 1\,\text{mm}$ value is only a point read from the sensitivity curve, not a value declared by the original Methodology B.

TABLE XV
COMPARISON OF THE MODELING LEVELS.

Model	P_{Cu} (W)	total loss (W)	η_{tr} (%)
Original Methodology B	4.551	5.524	78.36
Harmonic Dowell model (40th)	4.287	5.260	79.18
Harmonic + 2D at $d_g = 1$ mm	4.392	5.364	78.85

Interpretation of the Three Modeling Levels

The value obtained using Methodology B remains the project's reference, while the extensions demonstrate how the temporal and spatial distributions of the fields can alter the estimate without compromising the traceability of the initial method.

VI. NUMERICAL METHOD

Fig. 13 shows the geometry studied and problem's boundary, which will be defined according to the study to be carried out, including electrostatic, magnetostatic and thermostatic analysis.

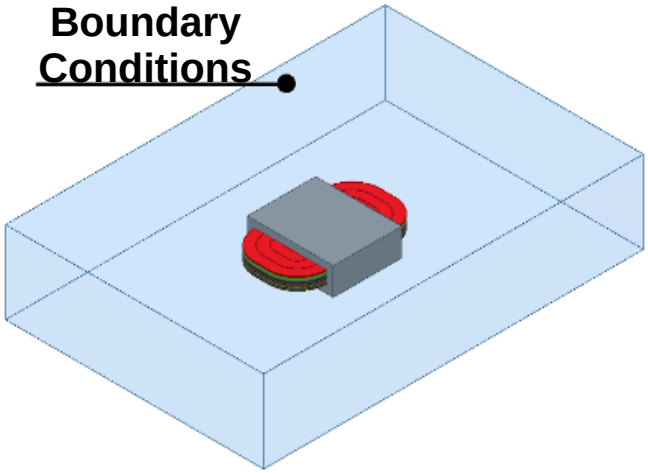


Fig. 13. Geometry and Boundary conditions of the Studied Problem, Applicable to Electrostatic, Magnetostatic and Thermal Analyses.

The boundary conditions are shown in Table XVI.

TABLE XVI
BOUNDARY CONDITIONS

Study	**Boundary condition**	**Value**
Electrostatic	Electric scalar potential	$V = 0$
Magnetostatic	Magnetic potential	$\vec{A} = 0$
Thermal	Border temperature	$T = 22\,C$

The quantities in electrostatic problems are specifically the electric field vectors $\vec{E}$ and electric flux density $\vec{D}$. The equation in electrostatics regime is:

$$-\epsilon\ \nabla^2\ V = \sigma. \tag{55}$$

In (55), V is the electric scalar potential, σ is the charge density and ϵ is the material's relative permittivity. The electrostatic study was necessary because, once the number of tracks

(turns), the number of layers and their dimensions had been determined, there was no guarantee that the voltage would be consistent across all tracks, since in certain flat converters, depending on the input and output voltage levels, the insulation may not be sufficient (low insulation between tracks). Low insulation can result in short circuits between tracks, which indicates very high potentials in them. In the simulation, it was found that the potentials obtained for each track did not vary significantly, indicating that there was no short circuit, which therefore demonstrated that the insulation was sufficient for this arrangement, according to Fig.14.

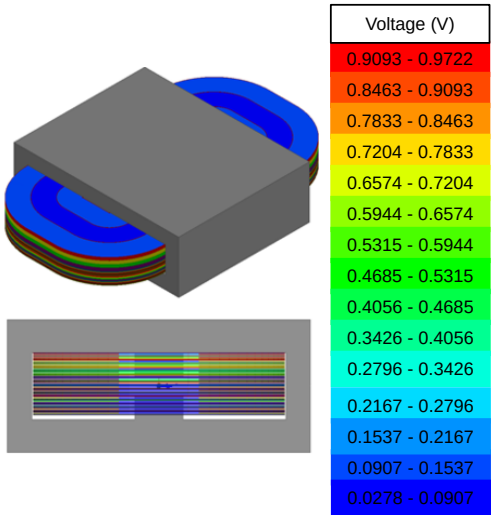


Fig. 14. Electrostatic Analysis of the Winding Tracks, Showing Sufficient Insulation Between Adjacent Turns.

In magnetostatic problem uses the vectors A, B, J and the relationship among these vectors can be seen in (56), where $\vec{J}$ is the current density vector, $\vec{A}$ is the magnetic potential vector and $\vec{B}$ is the vector flux density.

$$-\frac{1}{\mu(B)}\nabla^2\vec{A} = \vec{J} \tag{56}$$

With the core material selected, it was necessary to assess whether the magnetic saturation would remain within the design values, considering the nominal current values in both the primary and secondary windings. In the event of core saturation, the nominal voltage values may vary from the nominal values. In the simulation, it was found that the magnetic inductions in the core did not exceed saturation levels, remaining within the analytical value margin, as shown in Fig.15.

In thermal problems, the heat generation q within a given volume must be equal to the heat flow passing through the volume, i.e.:

$$-\nabla \cdot (k\nabla T) = q. \tag{57}$$

In (57), k is the material's thermal conductivity, T is the temperature and G is the gradient. The software solves (57) considering the *Dirichlet* boundary conditions. Fig.16.a) show the results of the thermal simulations on the core and Fig.16.b) show the results on the windings.

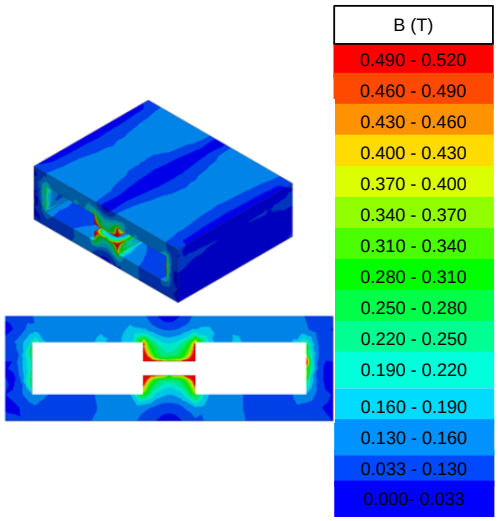


Fig. 15. Magnetostatic Analysis of the Core, Showing Magnetic Flux Densities Below Saturation Levels.

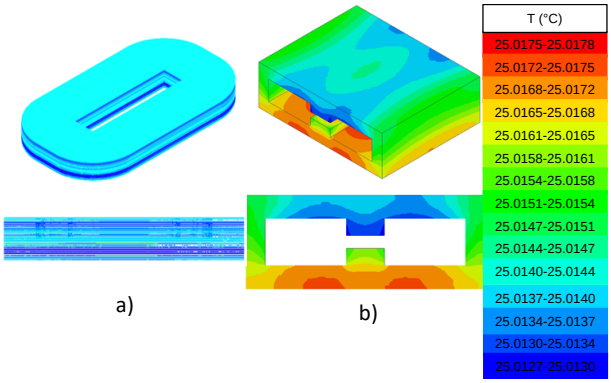


Fig. 16. Core Thermal and Windings Thermal Analysis - a) coil temperature b) core temperature.

Fig. 17.a) illustrates the skin effect at 100kHz on a track in the primary winding of the PTT. At the top are the flux lines and at the bottom are the colours indicating the levels of the current distributions. The effect of the proximity of two adjacent tracks in the primary winding is shown in Fig. 17.b). The magnetic inductions at 100kHz are plotted.

VII. Bench Tests on the Prototype

Fig. 18 illustrates the tests carried out on the prototype, to obtain the electrical resistances in DC, AC and transformation ratio, all at 25°C. The purpose of using three different values of N_p (A, B and C) was to check for possible inconsistencies in the measurements of N_s.

Table XVII shows the short-circuit test results, and Table XVIII shows the no-load test results.

A. Frequency Response Testing

Fig. 19 shows the frequency response test performed on the planar transformer's primary terminals and illustrates

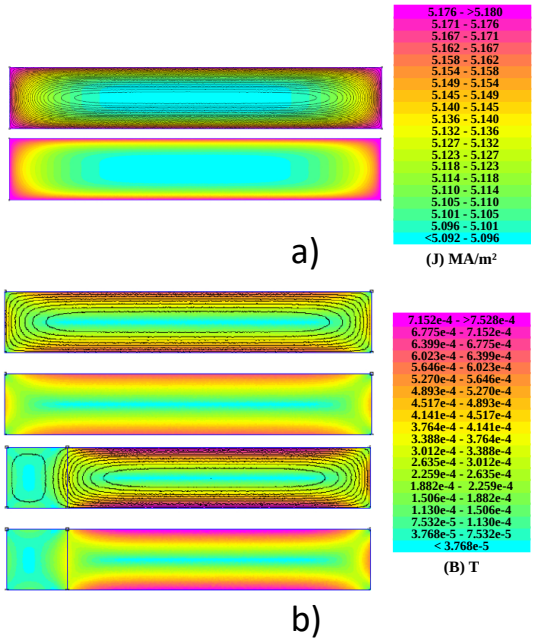


Fig. 17. Current Density Analysis and Induction with Proximity Effect - a) primary skin effect b) primary proximity effect.

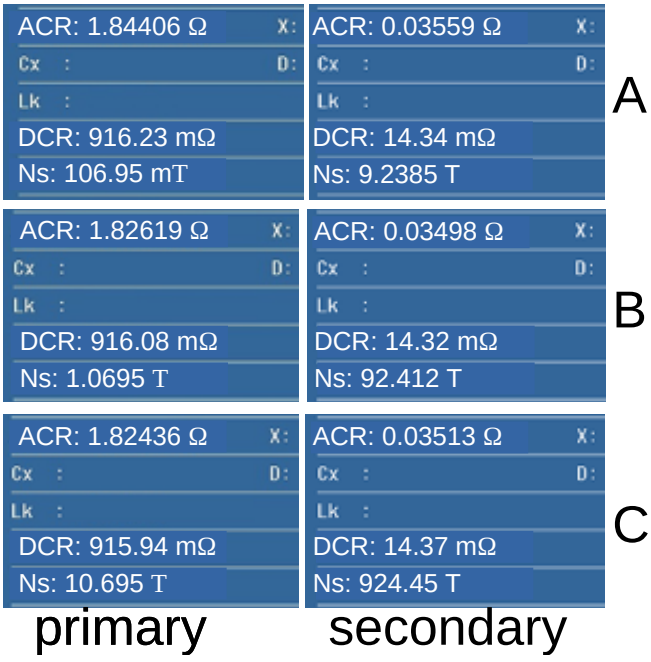


Fig. 18. Measured DC and AC Resistances of the Prototype at 25 °C for Three Different Values of N_p - a) 1st transformation relation b) 2nd transformation relation c) 3rd transformation relation.

the impedance $Z_{(\omega)}$ obtained from the measurement. The resonance frequency f_r, caused by the parasitic capacitance between windings, is well separated from the operating frequency, ensuring safe operation. Above this point, the component exhibits strongly capacitive characteristics.

TABLE XVII
SHORT-CIRCUIT RESULTS

Parameter	Results
Primary AC resistance - $R_{1(ac)}$	1.830 Ω
Secondary AC resistance reflected to primary - $R'_{2(ac)}$	3.047 Ω
Short-circuit resistance - R_{sc}	4.877 Ω
Primary leakage inductance - $L_{1(ac)}$	$0.79 \cdot 10^{-11}$ H
Secondary leakage inductance - $L'_{2(ac)}$	$0.79 \cdot 10^{-11}$ H
Short-circuit inductance - L_{sc}	$1.58 \cdot 10^{-11}$ H

TABLE XVIII
NO-LOAD TEST RESULTS

Parameter	Results
Equivalent resistance (core losses) — R_P	0.0561 Ω
Magnetizing inductance — L_m	9.17 μH

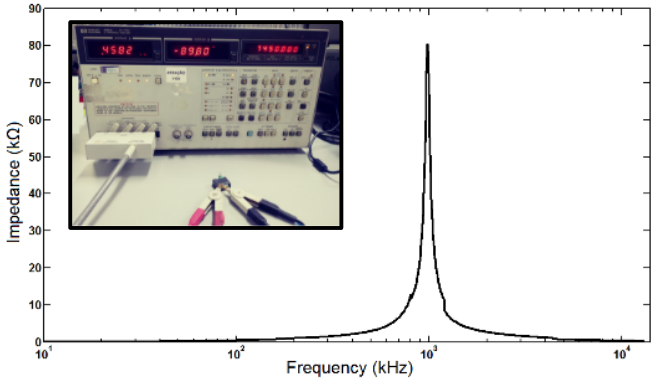


Fig. 19. Measured impedance $Z(\omega)$ at the primary terminals, showing the resonance frequency f_r well separated from the operating frequency.

B. Converter Waveforms

Fig. 20 shows the experimental bench used to perform the functional tests for the converter with an output voltage of $V_o = 10V$, using the designed PPT.

The primary switch waveform and the output ripple are shown in Fig.21a and Fig.21b, respectively.

VIII. CONVERTER DYNAMIC SIMULATION

Based on Tables XVII and XVIII, a dynamic simulation of the flyback-PTT converter was performed in PSIM to analyse the output voltage and current responses. Fig.22 shows the converter schematic, including its control loop.

Fig. 23 shows the converter's output voltage, which reaches 10V with negligible overshoot during the transient-to-steady transition. The operating-point ripple is 400mVpp.

Table XIX presents the converter control loop simulation parameters.

IX. CONCLUSION

This work presented a comparative analytical, numerical, and experimental investigation of two design methodologies for a planar transformer applied to a 20 W CCM flyback

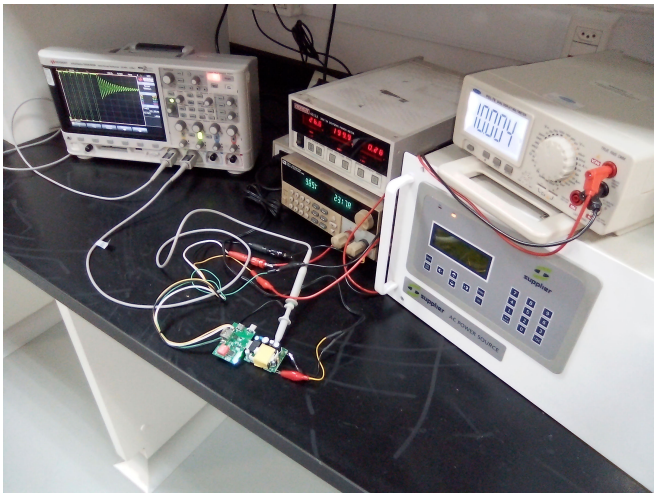


Fig. 20. Experimental Bench Used for the Functional Tests of the Converter With the Designed PTT at $V_o = 10\,\text{V}$.

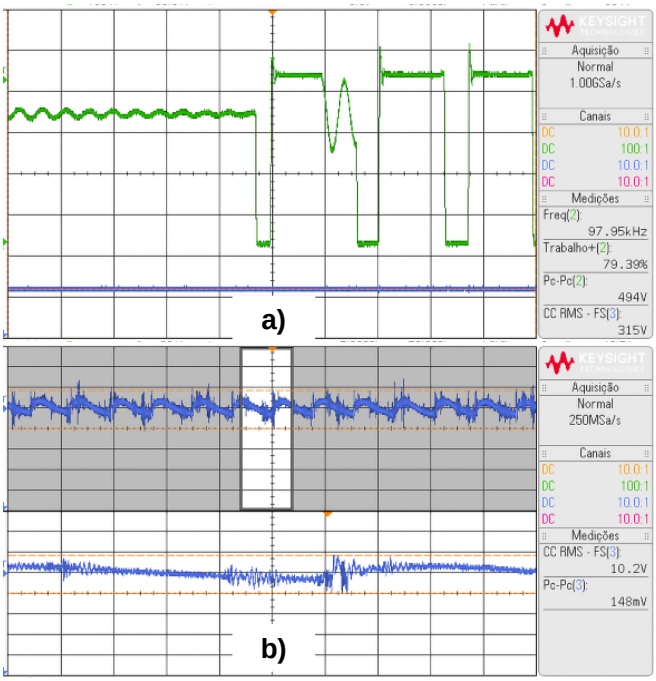


Fig. 21. Measured Voltage and Current Waveforms of the Primary Switch - a) primary switch b) output ripple

TABLE XIX
CONTROL LOOP PARAMETERS

Parameter		Parameter	
V_{ref}	2.5 V	R_2	19.9 kΩ
V_o	10.0 V	R_{2_i}	652.3 kΩ
$Gain$	0.25	R_{11}	10 kΩ
$Gain_i$	1 Ω	R_{11_i}	10 kΩ
$Gmod_i$	1	C_2	2.24 nF
f_{sw_i}	100 kHz	C_{2_i}	10.36 nF
f_{pole}	20 kHz	—	—

converter operating at 100 kHz. Methodology A is primarily based on determining a minimum magnetic-core size from the required power-processing capability, whereas Methodology B introduces an explicit relationship among core-loss density, magnetic flux density, material characteristics, core volume, and allowable temperature rise. This thermal-loss constraint provides a more physically meaningful criterion for selecting the magnetic material and core geometry, particularly when manufacturer data alone are insufficient for a complete planar-transformer design. For the investigated operating point, Methodology B resulted in an E32/6/20 core with an effective volume of 5.38 cm^3, compared with 5.75 cm^3 obtained with Methodology A, corresponding to a 6.43% reduction in magnetic-core volume. This reduction confirms the potential of the Type B procedure for increasing power density. Nevertheless, the present results also demonstrate that this improvement should not be interpreted simply as evidence of a globally optimized transformer. The calculated core-loss density of 180.8 mW/cm^3 is very close to the admissible value of 181.1 mW/cm^3, corresponding to approximately 99.83% of the core-loss limit established by the adopted thermal criterion. Therefore, the smaller magnetic structure is obtained at the expense of a relatively small core-loss margin. This observation is important because uncertainties in material properties, manufacturing tolerances, operating temperature, and excitation conditions may reduce the practical margin available in the final device. A more significant result emerges from the detailed loss analysis. The Type B design presents approximately 0.973 W of core loss and 4.551 W of winding loss, resulting in a total transformer loss of 5.524 W at the nominal operating point. Consequently, only 17.61% of the total loss is associated with the ferrite core, whereas 82.39% occurs in the planar windings. The primary winding alone accounts for approximately 59.75% of the total transformer loss. These results indicate that, once an appropriate low-loss ferrite has been selected, further reductions in core volume or core-loss density have limited impact on the total efficiency unless the winding structure is simultaneously optimized. The decomposition of the winding losses reinforces this conclusion. Approximately 2.147 W is associated with the DC-resistance baseline, only 0.120 W with the additional skin-effect contribution, and approximately 2.284 W with the estimated proximity-effect contribution. Thus, the proximity effect represents approximately 41.35% of the total transformer losses and becomes one of the dominant high-frequency loss mechanisms in the investigated planar structure. This result demonstrates that conductor thickness alone is not sufficient to guarantee low AC resistance. Layer arrangement, conductor width, spacing between turns, magnetic-field distribution, and primary-to-secondary arrangement become critical design variables. Therefore, the major opportunity for improving the present transformer is not necessarily the use of a different ferrite core, but rather the optimization of the planar winding geometry and its electromagnetic interaction. The resulting analytical transformer-only efficiency is 78.36%, considering 20 W delivered to the output stage. Although this value confirms the functional feasibility of the proposed transformer, it also shows that the present design is not yet optimized from an efficiency perspective. More importantly, the value should not be confused with the overall flyback-converter efficiency,

since semiconductor switching and conduction losses, rectifier losses, snubber losses, gate-drive consumption, capacitor ESR losses, and auxiliary-circuit consumption were not included. The efficiency therefore serves primarily as a quantitative indicator of the electromagnetic component itself and clearly identifies where redesign efforts should be concentrated.

An important consistency check was obtained by replacing the analytical winding resistances with the measured values. The resulting estimated transformer efficiency was approximately 78.14%, differing from the analytical value by only 0.22 percentage points. This close agreement supports the usefulness of the proposed analytical loss model at the investigated operating point. However, it should not be interpreted as a complete experimental validation of each individual loss mechanism. In particular, the proximity-effect contribution was inferred from the difference between measured AC resistance and the estimated skin-effect contribution rather than measured independently. Therefore, agreement in total resistance does not necessarily imply that the individual skin- and proximity-effect components are predicted with the same accuracy.

The experimental characterization further supports the feasibility of the selected geometry. The measured transformation ratio, magnetizing behavior, short-circuit response, and frequency response were consistent with the intended operation of the transformer. In particular, the first significant resonance was observed around the 1 MHz range, approximately one decade above the 100 kHz switching frequency. Therefore, the transformer operates predominantly in its inductive region at the nominal switching frequency, reducing the influence of parasitic resonance on the intended operating point. The dynamic converter simulation using experimentally obtained transformer parameters also reproduced the regulated 10 V output, indicating that the designed magnetic component can be consistently incorporated into the closed-loop flyback model.

The main contribution of the proposed approach is therefore not only the comparison between two core-sizing procedures, but the establishment of a design sequence that connects analytical sizing, magnetic-material selection, planar-winding design, high-frequency loss estimation, three-dimensional field analysis, prototype characterization, and converter-level simulation. This integrated procedure makes explicit several quantities that are frequently treated separately in manufacturer-oriented design approaches and provides a reproducible path for identifying the physical mechanisms that limit planar-transformer performance.

At the same time, the results reveal an important limitation of the Type B methodology in its present form: the thermal constraint is predominantly used to size the magnetic core, while the final transformer performance is dominated by winding losses. Therefore, minimizing core volume alone does not necessarily maximize transformer efficiency or power density. A more comprehensive design strategy should simultaneously consider core loss, DC and AC winding losses, leakage inductance, parasitic capacitance, thermal resistance, insulation requirements, manufacturability, and total volume.

Overall, the study demonstrates that Methodology B provides a useful and more thermally informed starting point for planar-transformer sizing and enables a reduction in magnetic-core volume compared with Methodology A. However, the detailed loss analysis leads to the broader conclusion that the main design bottleneck of the investigated transformer is no longer the ferrite core but the planar winding system.

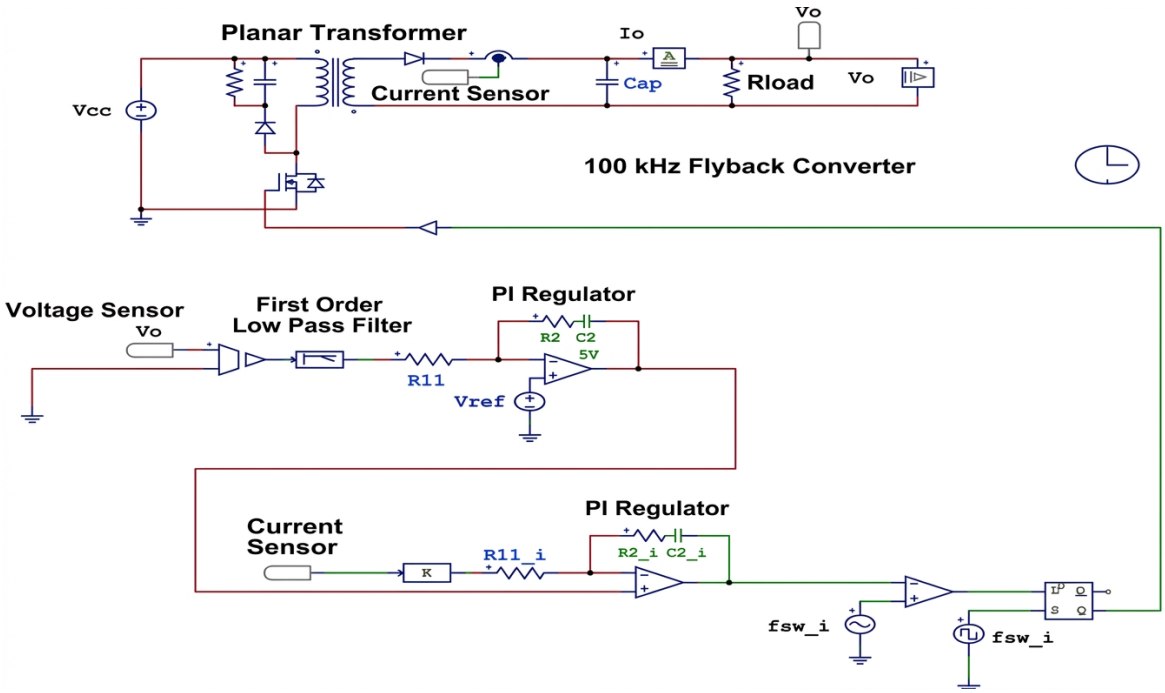


Fig. 22. Schematic of the flyback converter with the designed PTT, including the control loop, implemented in PSIM.

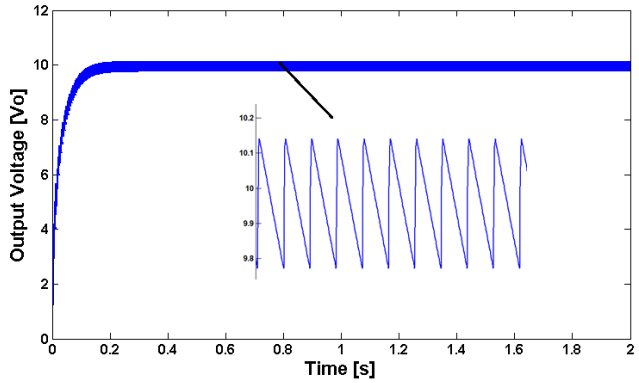


Fig. 23. Measured output voltage of the converter, reaching 10 V with 400 mV_{pp} ripple at steady state.

REFERENCES

[1] S. Oliver, "GaN power ICs enable the new revolution in power electronics." EE Power, Technical Article, Feb. 2018. [Online]. Available: https://eepower.com/technical-articles/gan-power-ics-enable-the-new-revolution-in-power-electronics/. Accessed: Jul. 30, 2026.

[2] M. Ahmad, "A brief history of gallium nitride (GaN) semiconductors." EDN, May 2023. [Online]. Available: https://www.edn.com/a-brief-history-of-gallium-nitride-gan-semiconductors/. Accessed: Jul. 30, 2026.

[3] Y. Zhong, J. Zhang, S. Wu, L. Jia, X. Yang, Y. Liu, Y. Zhang, and Q. Sun, "A review on the GaN-on-Si power electronic devices," *Fundamental Research*, vol. 2, pp. 462–475, May 2022. doi: 10.1016/j.fmre.2021.11.028.

[4] F. Dostal, "Considerations for using gallium nitride technology in switch-mode power supplies." Analog Dialogue, Analog Devices, Apr. 2025. [Online]. Available: https://www.analog.com/en/resources/analog-dialogue/articles/considerations-for-using-gallium-nitride-technology.html. Accessed: Jul. 30, 2026.

[5] A.-C. Liu, P.-T. Tu, C. Langpoklakpam, Y.-W. Huang, Y.-T. Chang, A.-J. Tzou, L.-H. Hsu, C.-H. Lin, H.-C. Kuo, and E. Y. Chang, "The evolution of manufacturing technology for GaN electronic devices," *Micromachines*, vol. 12, p. 737, Jun. 2021. doi: 10.3390/mi12070737.

[6] J. S. McLean, "Guanella transformer/balun implemented with planar transformer technology," in *2022 IEEE Texas Symposium on Wireless and Microwave Circuits and Systems (WMCS)*, vol. 2022, pp. 1–6, 2022. doi: 10.1109/WMCS55582.2022.9866125.

[7] L. Ma, F. Ren, Q. Li, and W. Gao, "Study of ac resistance calculation in equivalent networks of transformer windings and frequency response considering proximity effect," in *2023 IEEE 4th International Conference on Electrical Materials and Power Equipment (ICEMPE)*, vol. 2023, pp. 1–4, 2023. doi: 10.1109/ICEMPE57831.2023.10139726.

[8] P. Sojka, M. Pipiska, and M. Frivaldsky, "Gan power transistor switching performance in hard-switching and soft-switching modes," in *2019 20th International Scientific Conference on Electric Power Engineering (EPE)*, vol. 2019, pp. 1–5, 2019. doi: 10.1109/EPE.2019.8778060.

[9] Y. A. Wang, D. M. Xiao, and Y. L. Liu, "Design of a planar power transformer for high voltage, high frequency use," in *IEEE PES T&D 2010*, pp. 1–6, 2010. doi: 10.1109/TDC.2010.5484361.

[10] N. Dai, A. Lofti, C. Skutt, W. Tabisz, and F. Lee, "A comparative study of high-frequency, low-profile planar transformer technologies," in *Proceedings of 1994 IEEE Applied Power Electronics Conference and Exposition - ASPEC'94*, vol. 1994, pp. 226–232 vol.1, 1994. doi: 10.1109/APEC.1994.316395.

[11] D. van der Linde, C. Boon, and J. Klaassens, "Design of a high-frequency planar power transformer in multilayer technology," *IEEE Transactions on Industrial Electronics*, vol. 38, no. 2, pp. 135–141, 1991. doi: 10.1109/41.88907.

[12] J. S. N. T. Magambo, R. Bakri, X. Margueron, P. Le Moigne, A. Mahe, S. Guguen, and T. Bensalah, "Planar magnetic components in more electric aircraft: Review of technology and key parameters for dc–dc power electronic converter," *IEEE Transactions on Transportation Electrification*, vol. 3, no. 4, pp. 831–842, 2017. doi: 10.1109/TTE.2017.2686327.

[13] B. Rao, Y. Zhao, Y. Yang, J. Gao, Z. Zhang, S. Zhou, M. Zhang, and Z. Chen, "Reduction of leakage inductance and AC resistance of planar transformers by optimising the current distribution," *IET Power Electronics*, vol. 11, no. 3, pp. 501–506, 2018. doi: 10.1049/iet-pel.2017.0362.

[14] Z. Ouyang, O. C. Thomsen, and M. A. E. Andersen, "Optimal design and tradeoff analysis of planar transformer in high-power dc–dc converters," *IEEE Transactions on Industrial Electronics*, vol. 59, no. 7, pp. 2800–2810, 2012. doi: 10.1109/TIE.2010.2046005.

[15] Z. Ouyang and M. A. E. Andersen, "Overview of planar magnetic technology—fundamental properties," *IEEE Transactions on Power Electronics*, vol. 29, no. 9, pp. 4888–4900, 2014. doi: 10.1109/TPEL.2013.2283263.

[16] M. A. Saket, N. Shafiei, and M. Ordonez, "LLC converters with planar transformers: Issues and mitigation," *IEEE Transactions on Power Electronics*, vol. 32, no. 6, pp. 4524–4542, 2017. doi: 10.1109/TPEL.2016.2602360.

[17] F. Groon, H. Beiranvand, and M. Liserre, "In-depth review of planar transformer modeling and optimization: Challenges and perspectives," *IEEE Transactions on Power Electronics*, vol. 41, no. 4, pp. 5426–5448, 2026. doi: 10.1109/TPEL.2025.3622943.

[18] S. Nagao, K. Maruyama, I. Hirohama, and K. Yamasawa, "A new micro-switching regulator using a planar-type magnetic core," *IEEE Translation Journal on Magnetics in Japan*, vol. 5, no. 7, pp. 604–610, 1990. doi: 10.1109/TJMJ.1990.4564149.

[19] M. Mino, T. Yachi, A. Tago, K. Yanagisawa, and K. Sakakibara, "A new planar microtransformer for use in micro-switching converters," *IEEE Transactions on Magnetics*, vol. 28, no. 4, pp. 1969–1973, 1992. doi: 10.1109/20.144755.

[20] R. Prieto, O. Garcia, R. Asensi, J. Cobos, and J. Uceda, "Optimizing the performance of planar transformers," in *Proceedings of Applied Power Electronics Conference. APEC '96*, vol. 1, pp. 415–421 vol.1, 1996. doi: 10.1109/APEC.1996.500475.

[21] C. Ropoteanu, P. Svasta, and I. Buşu, "High-frequency power loss investigation of a planar ferrite core transformer," in *2015 IEEE 21st International Symposium for Design and Technology in Electronic Packaging (SIITME)*, vol. 2015, pp. 61–64, 2015. doi: 10.1109/SIITME.2015.7342296.

[22] V. K. N., S. Satpathy, and L. N., "Analysis and design methodology for planar transformer with low self-capacitance used in high voltage flyback charging circuit," in *2016 IEEE International Conference on Power Electronics, Drives and Energy Systems (PEDES)*, vol. 2016, pp. 1–5, 2016. doi: 10.1109/PEDES.2016.7914510.

[23] J. Zhang, C. Liu, X. Zhao, and Y. Zhao, "Design of mhz level planar transformer and analysis of leakage and loss," in *2018 2nd IEEE Advanced Information Management,Communicates,Electronic and Automation Control Conference (IMCEC)*, vol. 2018, pp. 2697–2700, 2018. doi: 10.1109/IMCEC.2018.8469299.

[24] P. Ren, W. Chen, X. Huang, Y. Cao, Y. Chen, and X. Yang, "A low winding loss magnetic circuit structure design of planar inductor for gan-based totem-pole pfc," in *2021 IEEE Workshop on Wide Bandgap Power Devices and Applications in Asia (WiPDA Asia)*, pp. 417–422, 2021. doi: 10.1109/WiPDAAsia51810.2021.9656075.

[25] X. Zhou *et al.*, "A design method of partially interleaved winding structure with low leakage inductance for planar transformer application," *IEEE Transactions on Power Electronics*, vol. 38, no. 5, pp. 6366–6379, 2023. doi: 10.1109/TPEL.2023.3242109.

[26] T. Yuan, F. Jin, Z. Li, C. Zhao, and Q. Li, "Design of an integrated transformer with parallel windings for a 30-kw llc resonant converter," *IEEE Transactions on Power Electronics*, vol. 38, no. 11, pp. 14317–14333, 2023. doi: 10.1109/TPEL.2023.3291954.

[27] A. Nabih and Q. Li, "Design of 98.8% efficient 400-to-48-v llc converter with optimized matrix transformer and matrix inductor," *IEEE Transactions on Power Electronics*, vol. 38, no. 6, pp. 7207–7225, 2023. doi: 10.1109/TPEL.2023.3244869.

[28] F. Jin, A. Nabih, Z. Li, and Q. Li, "A scalable matrix integrated transformer with controllable leakage inductance for a bi-directional resonant converter," *IEEE Transactions on Power Electronics*, vol. 38, no. 9, pp. 10967–10984, 2023. doi: 10.1109/TPEL.2023.3270400.

[29] Z. Li, Y.-H. Hsieh, Q. Li, and F. C. Lee, "High-frequency transformer design with medium-voltage insulation for resonant converter in solid-state transformer," *IEEE Transactions on Power Electronics*, vol. 38, no. 8, pp. 9917–9932, 2023. doi: 10.1109/TPEL.2023.3279030.

[30] T. Yuan, F. Jin, and Q. Li, "Analysis and comparison of integrated planar transformers for 22-kw on-board chargers," *IEEE Transactions on Power Electronics*, vol. 39, no. 9, pp. 11368–11385, 2024. doi: 10.1109/TPEL.2024.3410878.

[31] D. Lee, H. P. Kieu, J. Kim, S. Choi, S. Kim, and W. Martinez, "A gan-based improved zeta converter with integrated planar transformer for 800-v electric vehicles," *IEEE Transactions on Industrial Electronics*, vol. 71, no. 12, pp. 15815–15825, 2024. doi: 10.1109/TIE.2024.3390728.

[32] R. Barzegarkhoo, F. Groon, A. Sengupta, and M. Liserre, "Wide voltage range reconfigurable dab converter realized by monolithic bidirectional gan/discrete sic-fets, and planar transformer," *IEEE Transactions on Power Electronics*, vol. 40, no. 11, pp. 17366–17383, 2025. doi: 10.1109/TPEL.2025.3587501.

[33] P. R. Prakash, A. Nabih, and Q. Li, "Termination design optimization of high-current pcb-winding matrix transformers," *IEEE Transactions on Power Electronics*, vol. 38, no. 4, pp. 4957–4971, 2023. doi: 10.1109/TPEL.2022.3230639.

[34] A. Nabih and Q. Li, "A method to embed resonant inductor into pcb matrix transformer for high-density resonant converters," *IEEE Transactions on Power Electronics*, vol. 39, no. 2, pp. 2385–2400, 2024. doi: 10.1109/TPEL.2023.3330974.

[35] A. Nabih, F. Jin, and Q. Li, "Efficient integrated transformer–inductor with high pcb utilization and optimized core," *IEEE Transactions on Industrial Electronics*, vol. 71, no. 6, pp. 5653–5662, 2024. doi: 10.1109/TIE.2023.3294637.

[36] F. Jin, A. Nabih, T. Yuan, and Q. Li, "A high-efficiency high-density three-phase cllc resonant converter with a universally derived three-phase integrated transformer for on-board-charger application," *IEEE Transactions on Power Electronics*, vol. 39, no. 4, pp. 4350–4366, 2024. doi: 10.1109/TPEL.2024.3354679.

[37] T. E. Hajji, S. Hlioui, F. Louf, M. Gabsi, G. Mermaz-Rollet, and M. Belhadi, "Hybrid model for ac losses in high speed pmsm for arbitrary flux density waveforms," in *2020 International Conference on Electrical Machines (ICEM)*, vol. 1, pp. 2426–2432, 2020. doi: 10.1109/ICEM49940.2020.9271017.

[38] A. Ammouri, T. B. Salah, and F. Kourda, "Modeling and simulation of a high-frequency planar power transformers," in *2015 4th International Conference on Electrical Engineering (ICEE)*, pp. 1–6, 2015. doi: 10.1109/INTEE.2015.7416677.

[39] X. Nan and C. Sullivan, "An improved calculation of proximity-effect loss in high-frequency windings of round conductors," in *IEEE 34th Annual Conference on Power Electronics Specialist, 2003. PESC '03.*, vol. 2, pp. 853–860 vol.2, 2003. doi: 10.1109/PESC.2003.1218168.

[40] G. Bertotti, "General properties of power losses in soft ferromagnetic materials," *IEEE Transactions on Magnetics*, vol. 24, no. 1, pp. 621–630, 1988. doi: 10.1109/20.43994.

[41] Ferroxcube, *Design of Planar Power Transformers*, 1997. Accessed: July 26, 2024. [Online].

[42] C. McLyman, *Transformer and Inductor Design Handbook (4th ed.)*. CRC Press, 2011. doi: 10.1201/b10865.



Gabriel R. Bruzinga received his B.Sc. in Energy Engineering from the Universidade Federal do ABC (UFABC), and his M.Sc. in Electrical Engineering and Ph.D. in Energy from the same university. His research focuses on projects involving permanent magnet synchronous generators (PMSGs) for wind power and motors for electric vehicles.



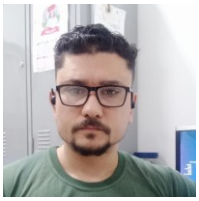
Ademir Pelizari received his B.Sc. in Electrical Engineering from the Universidade de Mogi das Cruzes (UMC), and his M.Sc. (2009) and Ph.D. (2015) degrees. He currently serves as an Adjunct Professor at the Universidade Federal do ABC (UFABC), working in the areas of electromechanical devices and electrical machines.



José Alberto Torrico Altuna received his B.Sc. in Electronic Engineering from the National University of Engineering, Lima, Peru (1986), and his M.Sc. (1997) and Ph.D. (2002) degrees in Electrical Engineering from the State University of Campinas (UNICAMP). He also completed a postdoctoral degree from CAPES (2013–2015) at the Universidade Federal do ABC (UFABC).



Alfeu Sguarezi Filho received his Ph.D. in Electrical Engineering from the State University of Campinas (UNICAMP). He currently serves as a Professor at the Universidade Federal do ABC (UFABC). He is a Senior Member of the IEEE and the author of articles and book chapters in the areas of electrical machines, control, power electronics, and wind energy.



Vinícius Graias holds a degree in Mechanical Manufacturing and a degree in Pedagogy, as well as a postgraduate degree in Maintenance Engineering. He is a Mechatronics Technician at the Universidade Federal do ABC (UFABC), and he works with equipment maintenance, metrology, and teaching at SENAI, combining industrial practice and technical education.